

# Wideband Radar Cross Section Reduction Using Artificial Magnetic Conductor Checkerboard Surface

Vadakkalathil A. Libi Mol\* and Chandroth K. Aanandan

**Abstract**—This paper presents a combinatorial triangle type artificial magnetic conductor checkerboard surface for wideband radar cross section reduction. The structure consists of a combination of a single band and dual band AMC unit cells with  $180\pm 37^\circ$  phase difference from 4.06 GHz to 11.2 GHz. 10 dB RCS reduction compared to PEC surface is realized from 4.4 GHz to 11.68 GHz (91%) for the proposed structure. The performance of the structure is compared with the conventional checkerboard surface. The distribution of scattered fields from both the structures are analyzed using array theory. The angular stability of the structures are also studied for TE and TM polarized wave incidences. A prototype of the proposed structure is fabricated, and the measured data are in good agreement with simulated results.

## 1. INTRODUCTION

Radar cross section (RCS) is the measure of detectability of the target when illuminated by an electromagnetic wave; i.e., it is the ratio of the backscattered power from the target in the direction of the radar to the power intercepted by the target. The research on RCS reduction techniques has a lot of impact in the military field. RCS of a target can be reduced by applying radar absorbing material or by redirecting the scattered wave away from the observer [1].

Artificial magnetic conductors are metamaterials with reflection phase varying from  $+180^\circ$  to  $-180^\circ$  and exhibiting in-phase reflection property (Phase =  $0^\circ$ ) at the resonance frequency [2]. At this frequency, AMC offers a very high impedance and can be considered as the dual of perfect electric conductor. Due to this characteristic, it has found many applications in antenna engineering [3, 4]. It is also used to design electromagnetic absorbers or scatterers to reduce the RCS. AMC consists of a layer of frequency selective surfaces (FSS) over the grounded dielectric. By imparting losses to FSS layer or dielectric, the impedance of the structure can be reduced to that of free space and can be used as an electromagnetic absorber [5–9].

A checkerboard surface consisting of AMC surface with in-phase reflection property and PEC with out of phase reflection property is used to destructively interfere the reflected power to achieve a null in the boresight direction, i.e., RCS reduction. The reflected power is scattered in different directions depending on the characteristics of the surface. This combination provides destructive interference at a single frequency and thus exhibits narrowband RCS reduction. Paquay et al. proposed such a checkerboard surface with 10 dB RCS reduction bandwidth of 5.82% [10]. The bandwidth of operation can be enhanced by replacing the PEC with another AMC surface so that the phase cancellation or destructive interference can be achieved over a wide frequency band. The chessboard combination formed by combining two different arrays of Jerusalem cross type AMC structures realized 40% frequency bandwidth with RCS reduction greater than 10 dB [11]. Chen et al. proposed square and hexagonal checkerboard surfaces with 10 dB reduction bandwidth of over 60% [12]. Chen et al. also

---

*Received 3 March 2018, Accepted 29 May 2018, Scheduled 18 June 2018*

\* Corresponding author: Vadakkalathil Abdul Hakim Libi Mol (libi.riyaz@gmail.com).

The authors are with the Department of Electronics, Cochin University of Science and Technology, Kerala, India.

proposed a dual frequency band checkerboard surface with 10 dB RCS reduction bandwidth of 61% and 24% [13]. A combinatorial triangle type AMC structure composed of two types of Jerusalem cross shaped structure, exhibiting peak value of scattered field reducing more than 5 dB compared to the conventional checkerboard structure is proposed by Hong et al. [14]. Zhuang et al. proposed another triangle type AMC structure with 10 dB RCS reduction bandwidth of 71.9% [15]. Cui et al. proposed the concept of coding metasurfaces in which the different unit cells with different phase responses mimicking different binary codes are arranged in sequence to manipulate the EM waves [16]. Liu et al. proposed a diffuse metasurface based on ergodic algorithm optimization to provide 10 dB RCS reduction bandwidth from 5.4 to 7.4 GHz [17]. A coding metasurface composed of a perfect metamaterial absorber and wideband artificial magnetic conductor is proposed to provide the 6-dB RCS reduction from 6.28 GHz to 9.16 GHz and from 6.33 GHz to 9.41 GHz under TE and TM polarized normal incident waves, respectively [18]. A novel strategy to realize a wide angle and polarization independent diffusion metasurface to provide RCS reduction in wider bandwidth is proposed by Zhuang et al. [19]. Artificial surface consisting of periodic elements with large periodicities can also be employed to excite higher number of harmonics and to achieve wideband scattering diffusion [20]. Coding phase gradient metasurface (CPGM) based on Pancharatnam-Berry phase is proposed to provide wideband wide angle RCS reduction [21].

A combinatorial triangle checkerboard surface for wideband RCS reduction (91%) is presented in this paper. The design complexity of this structure is less than the coding metasurfaces. The structure consists of two types of AMC cells: AMC-I (cross patch) and AMC-II (cross loop) exhibiting phase cancellation over a wider bandwidth (93.5%). The wideband phase cancellation is achieved by using single band (AMC-I) and dual band (AMC-II) AMC combination [22]. The performance of the structure is compared with a conventional checkerboard structure. The angular stability of the structures is also studied. A prototype of the proposed structure is fabricated, and the measured results are in good agreement with the simulations.

## 2. THEORETICAL ANALYSIS OF CHECKERBOARD SURFACES

The working mechanism of checkerboard surfaces can be explained by either coupling resonances [23, 24] concept or array factor theory [14, 15, 25].

### 2.1. Coupling Resonance Concept

The coupling resonance concept can be used to explain the RCS reduction performance when the AMC elements have overlapping operation bandwidth or not. In an ideal case, to obtain a perfect destructive interference from the chessboard structure, the reflection coefficient magnitude of both AMC elements should be 1, and the phase difference between the AMCs should be  $180^\circ$ . When the AMC elements have overlapping operation bandwidth, the surface can contribute higher RCS reduction performance. The enhanced RCS reduction bandwidth can be obtained by using elements with optimum frequency separation [23, 24]. In practical case, the magnitude of AMC elements is usually less than 1 due to dielectric losses. It is stated that even if the phase difference between the elements is not  $180^\circ$ , the chessboard surface can provide high RCS reduction when both the elements have same reflection coefficient magnitude.

### 2.2. Array Factor Theory

The array factor theory is best suitable to explain the RCS reduction performance of the chessboard structure when the bands of operation of AMC elements are not overlapping. To understand the enhancement in performance of combinatorial triangle type checkerboard (TCB) surface over the conventional chessboard structure (CCB), scattered fields from both the structures are analyzed. The configurations of CCB and TCB are shown in Figs. 1(a) and (b), respectively. It is assumed that both the AMC elements provide reflection coefficient magnitude of '1' in the entire frequency of operation. The CCB is considered as a rectangular array with  $180^\circ$  phase difference. In TCB, each grid is divided into four elements to enhance the RCS reduction property.

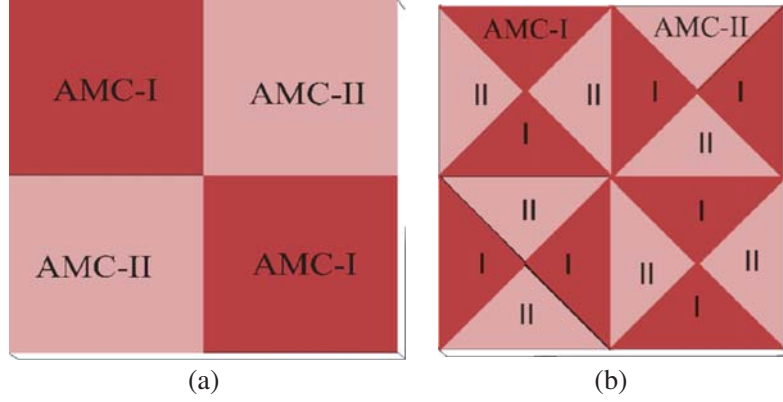


**Figure 1.** Unit cell configurations of (a) conventional checkerboard, (b) combinatorial triangle type chessboard.

The structure is considered as a planar array, and its array factor (F) is expressed as:

$$F_{total} = \sum_{m=0}^{M-1} \sum_{n=0}^{N-1} F_{mn}(\theta, \phi) = \sum_{m=0}^{M-1} \sum_{n=0}^{N-1} e^{jm\psi_x} e^{jn\psi_y} e^{j\phi_{mn}} \quad (1)$$

$$\psi_x = k\Delta x \sin(\theta) \cos(\phi) + \beta_x \quad (2)$$

$$\psi_y = k\Delta y \sin(\theta) \sin(\phi) + \beta_y \quad (3)$$

$$k = \frac{2\pi}{\lambda} \quad (4)$$

where  $M, N$  are the numbers of elements along  $X$  and  $Y$  axes;  $\Delta x$  and  $\Delta y$  are the spacing between the elements along  $X$  and  $Y$  axes;  $\theta$  and  $\phi$  are elevation and azimuth angles;  $\beta_x$  and  $\beta_y$  are the progressive phase shifts between the elements in  $X$  and  $Y$  directions;  $k$  is the wavenumber in free space.

The CCB consists of two types of AMC elements occupying half the area of total surface. The angle  $(\phi_0, \theta_0)$  along which the maximum scattering occurs is expressed as —

$$\tan \phi_0 = \frac{\beta_y \Delta x}{\beta_x \Delta y} \quad (5)$$

$$\sin^2 \theta_0 = \left( \frac{\beta_x}{k\Delta x} \right)^2 + \left( \frac{\beta_y}{k\Delta y} \right)^2 \quad (6)$$

The CCB unit cell consists of 4 AMC array blocks whereas TCB unit cell consists of 16 AMC array blocks. So for a fair comparison of array factors of CCB and TCB, CCB structure consisting of  $2 \times 2$  array of unit cells and TCB consisting of a single unit cell are considered. At the maximum RCS reduction frequency, the phase difference between the adjacent elements is  $180^\circ$ . So,  $e^{j\phi_{mn}}$  is represented by  $+1$  for AMC-I and  $-1$  for AMC-II. The array representation of CCB is shown in Fig. 2.

Thus the distribution  $e^{j\phi_{mn}}$  for CCB consisting of  $2 \times 2$  array of unit cells is expressed [15] as,

$$e^{j\phi_{mn}} = \begin{bmatrix} 1 & -1 & 1 & -1 \\ -1 & 1 & -1 & 1 \\ 1 & -1 & 1 & -1 \\ -1 & 1 & -1 & 1 \end{bmatrix} \quad (7)$$

The distribution of  $e^{j\phi_{mn}}$  for TCB cannot be expressed directly due to the triangular arrangement. The area is divided into  $6 \times 6$  square meshes as in Fig. 3. Based on the assumption that AMC-I and AMC-II provide destructive interference at the resonant frequency, the square mesh consisting of both types of AMCs is represented by 0. The square mesh consisting of AMC-I or AMC-II are represented by 1 and  $-1$ , respectively.

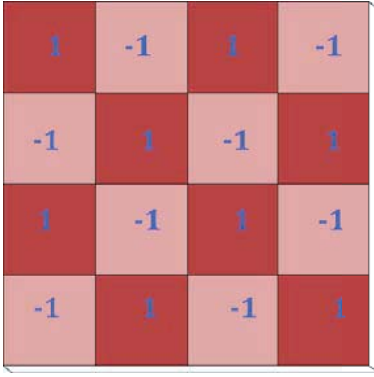


**Figure 2.** Array representation of  $2 \times 2$  CCB.

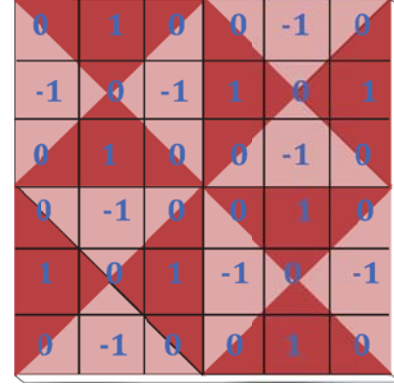


**Figure 3.** Array representation of TCB.

Thus the distribution  $e^{j\phi_{mn}}$  for TCB is expressed as,

$$e^{j\phi_{mn}} = \begin{bmatrix} 0 & 1 & 0 & 0 & -1 & 0 \\ -1 & 0 & -1 & 1 & 0 & 1 \\ 0 & 1 & 0 & 0 & -1 & 0 \\ 0 & -1 & 0 & 0 & 1 & 0 \\ 1 & 0 & 1 & -1 & 0 & -1 \\ 0 & -1 & 0 & 0 & 1 & 0 \end{bmatrix} \quad (8)$$

By substituting Equations (7) and (8) to Equation (1), the three-dimensional scattered fields for CCB and TCB are calculated using MATLAB and depicted in Figs. 4(a) and (b), respectively. For the CCB, four scattered main lobes are observed along the diagonal directions. For TCB, the number of main lobes is increased to eight, thus a reduction of peak scattered power is observed.

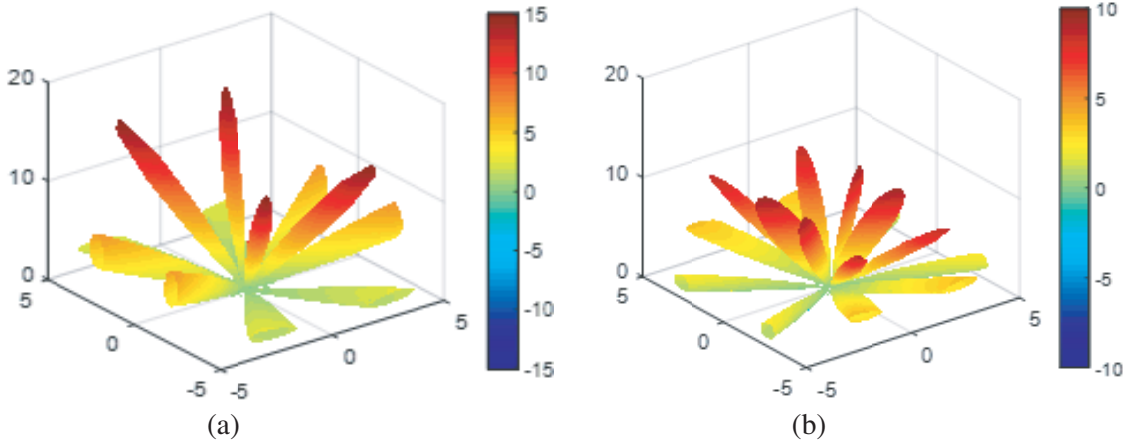


**Figure 4.** Calculated 3-D scattered field for (a) CCB, (b) TCB.

The RCS reduction of CCB compared to perfect electric conductor is represented by,

$$RCS \text{ reduction} = 10 \log \left[ \frac{\lim_{r \rightarrow \infty} \left[ \frac{4\pi r^2 |E^s|^2}{|E^i|^2} \right]}{\lim_{r \rightarrow \infty} \left[ 4\pi r^2 (1)^2 \right]} \right] = 10 \log \left[ \frac{|E^s|^2}{|E^i|^2} \right] \quad (9)$$

The checkerboard structure consists of two types of AMC elements occupying half the area of total surface. The total reflection coefficient can be approximated as the average of reflection coefficient of

both these elements. So the RCS reduction formula is approximated as

$$RCS\ reduction = 10 \log \left[ \frac{A_1 e^{jP_1} + A_2 e^{jP_2}}{2} \right]^2 \tag{10}$$

where  $A_1$  and  $A_2$  are the reflection coefficient magnitudes, and  $P_1$  and  $P_2$  are the reflection phases of two AMC elements. Equation (10) indicates that the 10 dB RCS reduction performance of the checkerboard surface occurs when the phase difference between the two AMC surfaces is within  $180 \pm 37^\circ$  given that the reflection coefficient magnitudes of both AMC elements are unity.

### 3. GEOMETRY OF THE STRUCTURE AND SIMULATED RESULTS

#### 3.1. AMC Design

To design a checkerboard surface for the desired RCS reduction, the structure must have proper combination of AMC elements. To avoid fabrication complexity, AMC elements without vias are considered. The unit cell geometry of the proposed AMC elements- AMC-I (cross patch) and AMC-II (cross loop) is illustrated in Fig. 5. The periodicities of both the elements are taken same to include the integer number of AMC elements on the checkerboard. These elements are located on the top of a metal backed Rogers RT/duroid substrate ( $\epsilon_r = 2.2$  and  $\tan \delta = 0.0009$ , thickness = 6.35 mm).

The simulation studies are carried out by using unit cell boundary conditions and floquet port excitation in CST MW Studio. The simulated reflection coefficient magnitude and phase of the AMC-I and AMC-II are shown in Fig. 6 and Fig. 7. The reflection coefficient magnitude is greater than 0.99 for both the structures, and the reduction in magnitude is due to dielectric and ohmic losses. The reflection phase of AMC-I shows resonance at 6.91 GHz. The bandwidth of operation of AMC-I is from 4.51 GHz to 9.5 GHz. The reflection phase of the AMC-II varies from  $+180^\circ$  to  $-180^\circ$  in two frequency bands with resonance frequencies at 3.81 GHz and 11.42 GHz. The bandwidth of operation of AMC-II is from 3.06 GHz to 4.4 GHz and from 10.25 GHz to 12.49 GHz.

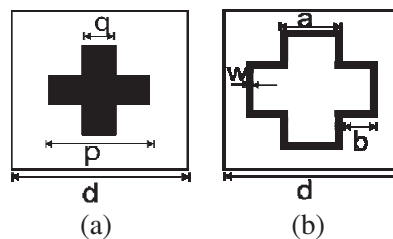


**Figure 5.** Geometry of the AMC unit cells. (a) AMC-I [ $d = 13$  mm,  $p = 7$  mm,  $q = 2.3$  mm]. (b) AMC-II [ $d = 13$  mm,  $w = 0.7$  mm,  $a = 5.5$  mm,  $b = 3.1$  mm].

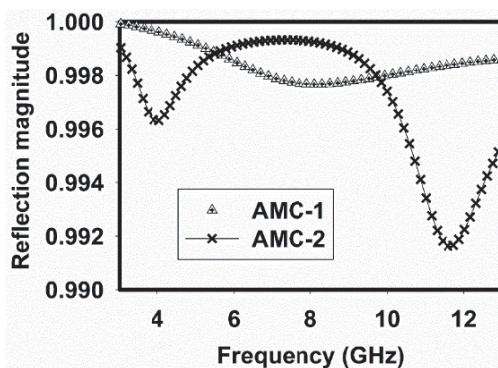


**Figure 6.** Reflection coefficient magnitude of AMC-I and AMC-II.

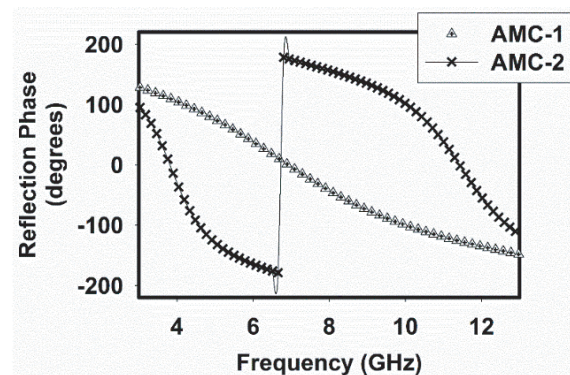


**Figure 7.** Reflection phases of AMC-I and AMC-II.

The angular stabilities of the AMC-I and AMC-II are also studied. The reflection phase and magnitude of AMC-I are shown in Figs. 8(a) and (b), respectively. The reflection characteristics of the structure changes with angle of incidence. AMC-I shows good angular stability up to  $10^\circ$  angle of incidence. The reflection phase and magnitude show large variation when angle of incidence is  $30^\circ$ . The reflection phase and magnitude of AMC-II are depicted in Figs. 9(a) and (b), respectively. AMC-II also shows angular stability up to  $10^\circ$ , and the reflection characteristics show variation with increase in angle of incidence.

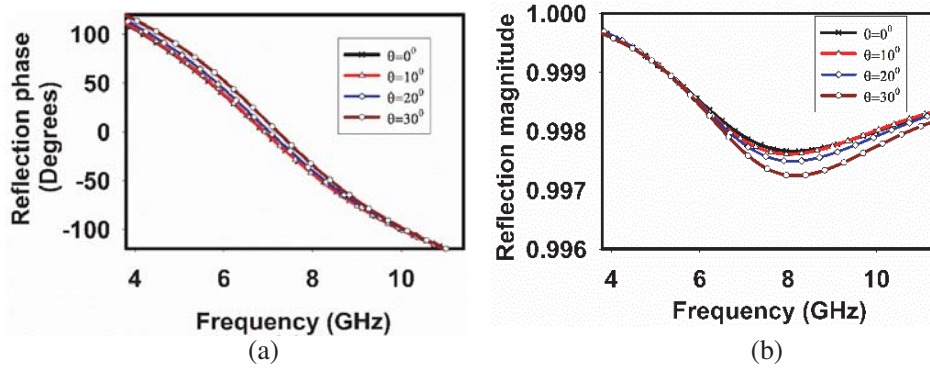


**Figure 8.** Simulated reflection characteristics of AMC-I for oblique incidence. (a) Phase. (b) Magnitude.

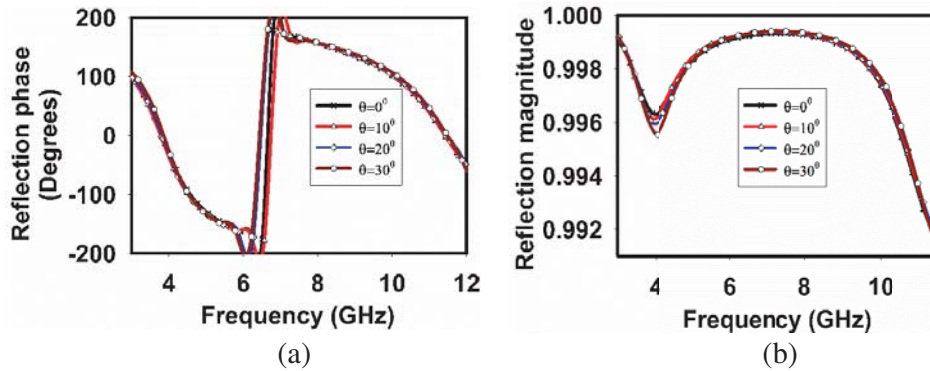


**Figure 9.** Simulated reflection characteristics of AMC-II for oblique incidence. (a) Phase. (b) Magnitude.

### 3.2. Checker Board Design

The AMCs can be arranged as checkerboard surface by conventional checkerboard patterning (CCB) or combinatorial triangle checkerboard (TCB) patterning. The considered conventional checkerboard consisting of  $2 \times 2$  unit cells and the triangle type checkerboard unit cell are shown in Figs. 10(a) and (b), respectively. The total dimension of the structure is  $208 \text{ mm} \times 208 \text{ mm}$ .

Since the structure does not have overlapping band of operation, the array factor theory is used here for explaining the RCS reduction performance. The phase difference between our proposed AMC-I and AMC-II is depicted in Fig. 11. It shows that the reflected power from AMC-I is out of phase with reflected fields from AMC-II at 4.435 GHz, 7.08 GHz and 10.61 GHz. At these frequencies, the scattered fields along the principal plane is destructively interfered, and fields will be scattered to other angles. The structure exhibits  $180 \pm 37^\circ$  phase difference from 4.06 GHz to 11.2 GHz and results in 10 dB RCS reduction in this frequency range.

The RCS reduction of conventional checkerboard surface as compared to the PEC surface is calculated using Equation (10) and illustrated in Fig. 12. The peak RCS reduction occurs at 4.42 GHz

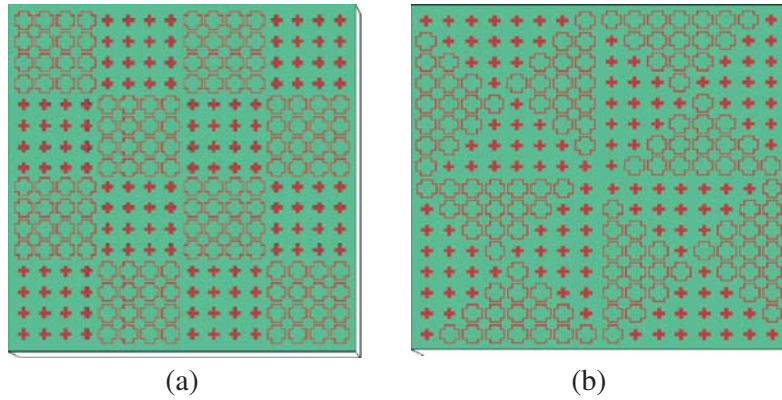


Figure 10. Considered (a) CCB, (b) TCB.

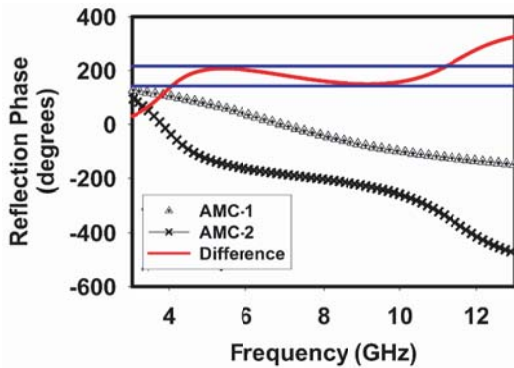


Figure 11. Unwrapped reflection phases of AMC-I, AMC-II and their difference.

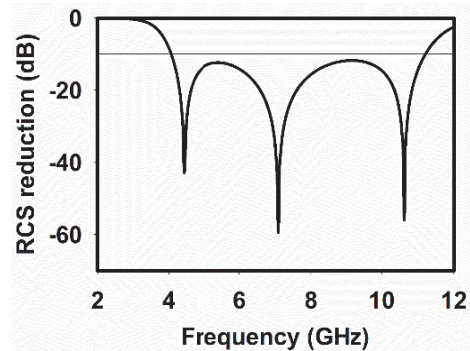


Figure 12. Approximated RCS reduction versus frequency for the checkerboard surface consisting of AMC-I and AMC-II.

(-42.34 dB), 7.09 GHz (-59.38 dB) and 10.62 GHz (-55 dB).

The RCS reduction performance of the checkerboard with variation in thickness of the substrate is shown in Fig. 13. The calculated fractional bandwidths are 4.2% and 93.5% for  $h = 3$  mm and 6.35 mm, respectively. The fractional bandwidths are 93.6% (lower frequency band) and 52.83% for  $h = 5$  mm. The depicted results indicate that the enhancement in bandwidth is mainly contributed by the increase in thickness of the substrate [26].

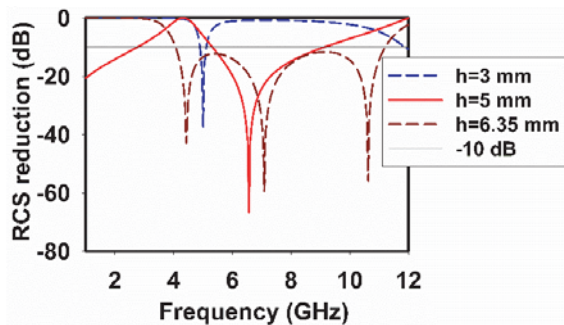


Figure 13. Approximated RCS reduction for different substrate thickness.

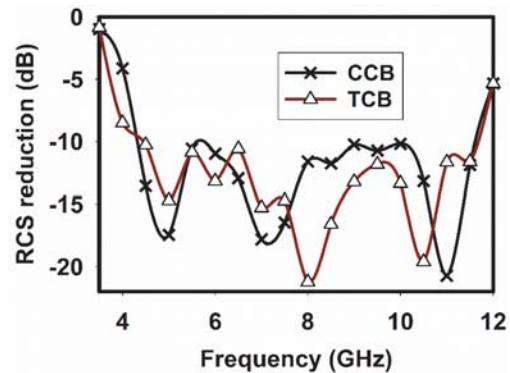


Figure 14. Simulated RCS reduction versus frequency for normal incidence.

The simulated RCS reduction versus frequency for the normal incidence is shown in Fig. 14. The CCB structure provides  $-10$  dB RCS reduction from 4.35 GHz to 11.53 GHz (90.42%). The CCB shows RCS reduction peaks at 5 GHz ( $-17.46$  dB), 7 GHz ( $-17.81$  dB) and 11 GHz ( $-20.74$  dB). The TCB provides  $-10$  dB reduction from 4.4 GHz to 11.68 GHz (91%) with peak RCS reduction at 5 GHz ( $-14.72$  dB), 8 GHz ( $-21.23$  dB) and 10.5 GHz ( $-19.61$  dB).

The 3-D bistatic patterns of the CCB and TCB surfaces at 10.5 GHz under normal incidence are shown in Figs. 15(a) and (b), respectively. It is indicated that the reflected power along the principal planes is negligible, and the reflected power is mainly distributed to  $\phi = 45^\circ, 135^\circ, 225^\circ$  and  $315^\circ$  planes for CCB structure. For TCB structure, the power is redistributed to  $\phi = 17^\circ, 73^\circ, 107^\circ, 163^\circ, 197^\circ, 253^\circ, 287^\circ$  and  $343^\circ$  planes. This agrees well with the predicted scattered fields using array theory. The maximum bistatic RCS of TCB surface (4.32 dB) is 3.06 dB less than that of CCB bistatic RCS (7.38 dB).

The scattered fields of the CCB along principal plane ( $\phi = 0^\circ$ ) and diagonal plane ( $\phi = 45^\circ$ ) as compared to the PEC plate are shown in Figs. 16(a) and (b), respectively. The RCS of the structure is reduced by 13.17 dB as compared to PEC in principal plane. Two major side lobe levels occur at  $\pm 34^\circ$ , and these power levels are 16.44 dB less than maximum RCS of the PEC plate. The scattered power is mainly concentrated at  $\theta = \pm 21^\circ$  along the diagonal plane ( $\phi = 45^\circ$ ), which is close to the predicted angle,  $\theta = 22.8^\circ$  (Equations (5) and (6)). The difference in the predicted and actual angles may be due

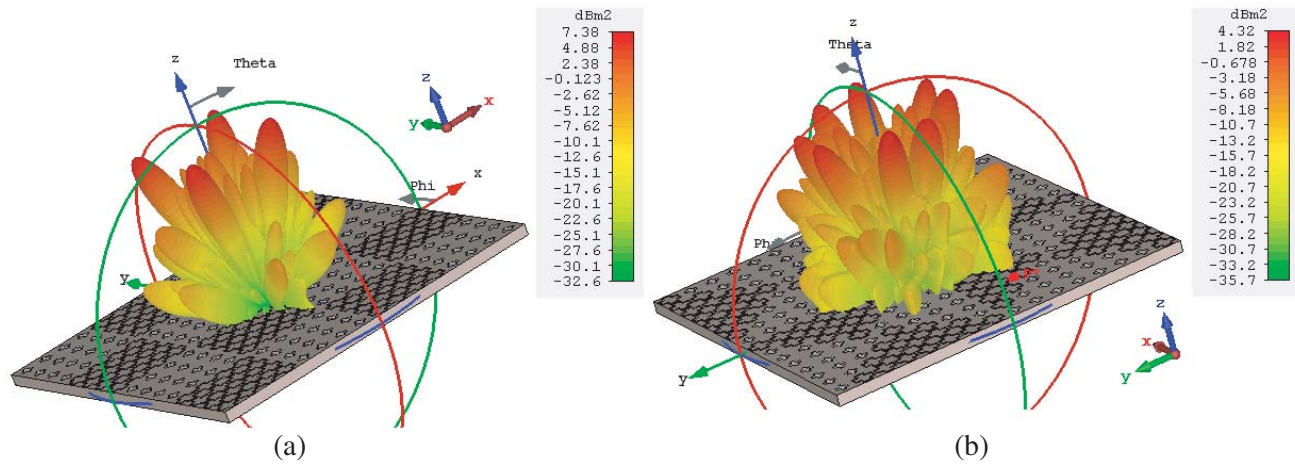


Figure 15. 3-D bistatic pattern under normal incidence at 10.5 GHz, (a) CCB, (b) TCB.

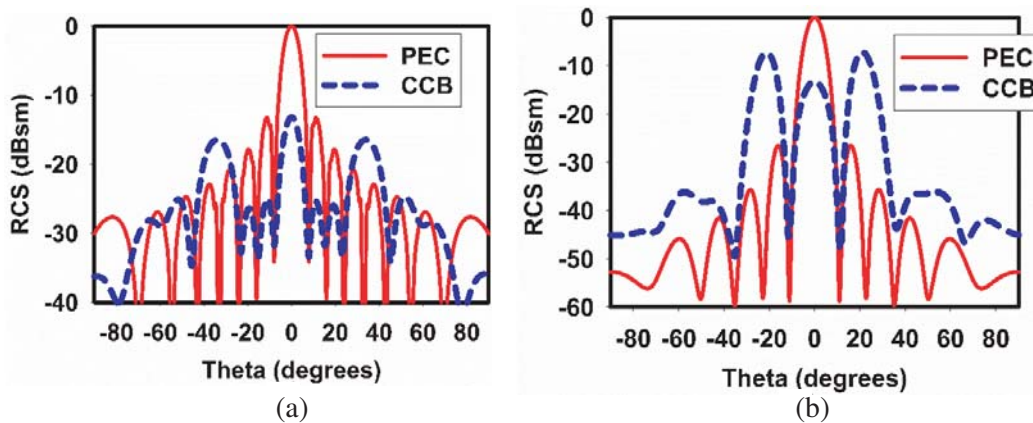
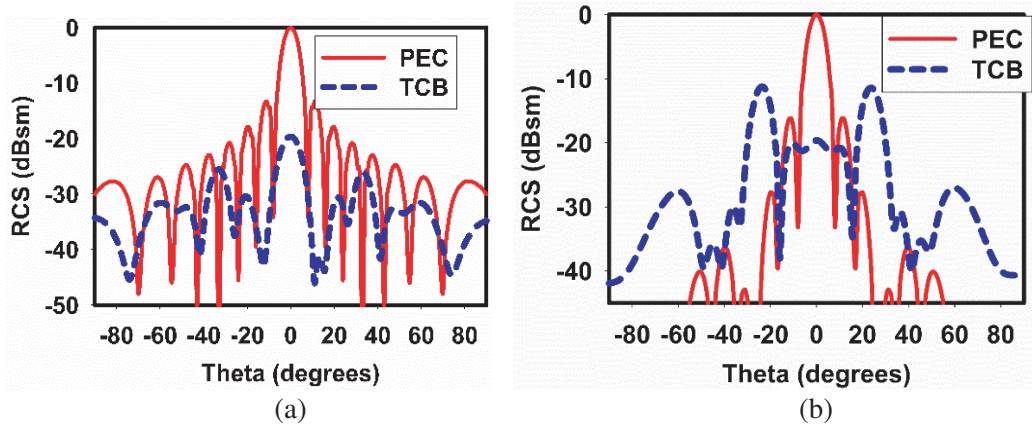


Figure 16. Bistatic RCS scattered field of CCB at 10.5 GHz as compared to PEC along (a)  $\phi = 0^\circ$ , (b)  $\phi = 45^\circ$ .

to edge diffraction. The peak RCS of the structure is reduced by 7.2 dB as compared to peak RCS of a similar PEC surface.

The scattered fields of the TCB along principal plane ( $\phi = 0^\circ$ ) and  $\phi = 17^\circ$  plane as compared to the PEC plate are shown in Figs. 17(a) and (b), respectively. The RCS of the structure is reduced by 19.6 dB as compared to PEC in principal plane. Along the  $\phi = 17^\circ$  plane, the scattered power is mainly concentrated at  $\theta = \pm 24^\circ$ . The maximum RCS along this plane is less than maximum RCS of the PEC surface by 11.26 dB.



**Figure 17.** Bistatic RCS scattered field of TCB at 10.5 GHz as compared to PEC along (a)  $\phi = 0^\circ$ , (b)  $\phi = 17^\circ$ .

Since the behavior of AMCs depends on the polarization and angle of incidence of the wave, the performance of the structures for oblique incidence under TE and TM polarized waves are presented. The RCS reduction offered by the CCB structure and TCB structure under oblique incidence for TE and TM polarized waves are shown in Fig. 18 and Fig. 19, respectively. Due to the rotational symmetry of CCB, it provides similar performances for TE and TM polarized wave incidences. The angular stabilities of both structures are summarized in Table 1. The RCS reduction bandwidth is decreased with angle of incidence, due to the dependence of the reflection characteristics of the structure on incident angle (Figs. 8 and 9). It is observed that the CCB structure provides better angular stability than TCB. The deterioration in the angular stability of TCB structure may be due to the overlapping arrangement of AMCs unit cells. In CCB, they are arranged periodically. The angular stability of the structure can be improved by using the loop based AMC unit cells [27].

The comparison of the performance of the structure with other wideband absorbers and Salisbury

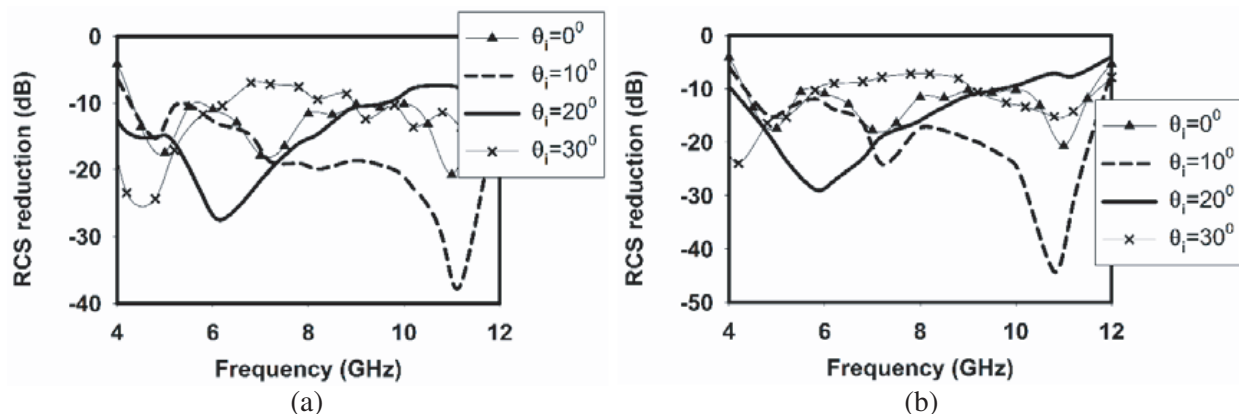


**Figure 18.** RCS reduction performance of CCB for different incident angles under (a) TE, (b) TM.

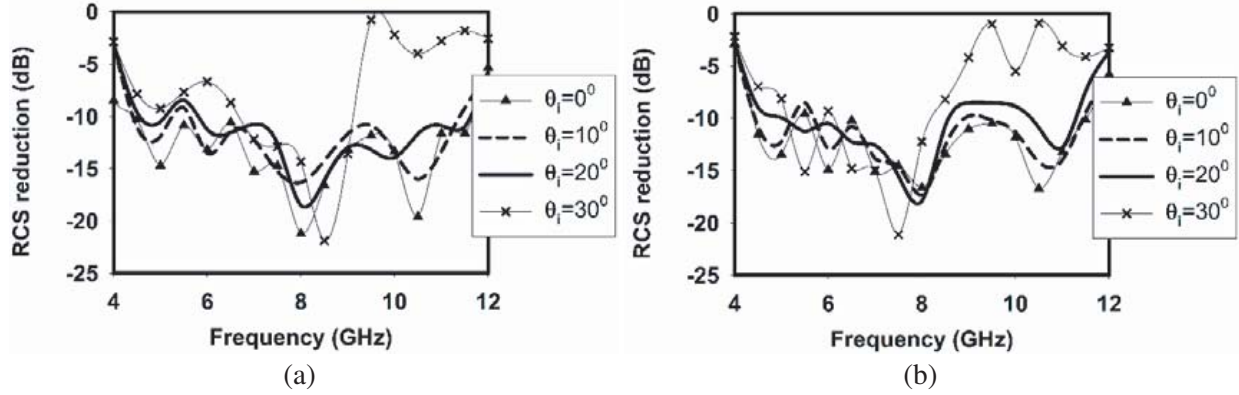


**Figure 19.** RCS reduction performance of TCB for different incident angles (a) TE, (b) TM.

**Table 1.** RCS reduction bandwidth for oblique incidence.

| Type of the structure | Angle of incidence (degrees) | RCS reduction bandwidth(%) - TE | RCS reduction bandwidth(%) - TM |
|-----------------------|------------------------------|---------------------------------|---------------------------------|
| TCB                   | 0                            | 91                              | 90.8                            |
|                       | 10                           | 18.18 and 64.3                  | 12.5, 37.2 and 16.4             |
|                       | 20                           | 64.3                            | 42.8 and 5                      |
|                       | 30                           | 28.5                            | 22.2                            |
| CCB                   | 0                            | 90.42                           | 90.42                           |
|                       | 10                           | 86                              | 86                              |
|                       | 20                           | 76.6                            | 76.6                            |
|                       | 30                           | 43.1, 27.4                      | 43.1, 4, 27.4                   |

**Table 2.** Comparison with other reported works.

| Ref.                  | Unit cell type | Frequency band (GHz) | Unit cell size (mm)     | Thickness (mm)            | 10 dB RCS reduction bandwidth (%) |
|-----------------------|----------------|----------------------|-------------------------|---------------------------|-----------------------------------|
| Salisbury screen      |                | 5.84–10.1            |                         | 6.33 ( $\lambda_h/3.16$ ) | 53.4                              |
| [11]                  | CCB            | 14.5–21.8            | 4 ( $\lambda_h/1.1$ )   | 1.27 ( $\lambda_h/3.48$ ) | 40.22                             |
| [12]                  | CCB            | 4.10–7.59            | 15 ( $\lambda_h/1.78$ ) | 6.35 ( $\lambda_h/4.2$ )  | 60                                |
| [14]                  | TCB            | 14.3–22.1            | 4 ( $\lambda_h/1.09$ )  | 1.27 ( $\lambda_h/3.44$ ) | 42.85                             |
| [15]                  | TCB            | 8.2–17.4             | 6 ( $\lambda_h/1.77$ )  | 3 ( $\lambda_h/3.54$ )    | 71.9                              |
| [22] — blended design | CCB            | 3.9–9.45             | 14 ( $\lambda_h/1.53$ ) | 6.35 ( $\lambda_h/3.37$ ) | 83                                |
| proposed              | TCB            | 4.4–11.68            | 13 ( $\lambda_h/1.33$ ) | 6.35 ( $\lambda_h/2.73$ ) | 91                                |
|                       | CCB            | 4.35–11.53           | 13 ( $\lambda_h/1.35$ ) | 6.35 ( $\lambda_h/2.76$ ) | 90.42                             |

screen is presented in Table 2, and it indicates that the proposed structure has wider 10 dB RCS reduction bandwidth compromising the thickness. The proposed TCB structure has slight enhancement in bandwidth as compared to the CCB.

#### 4. FABRICATION AND MEASUREMENT

To validate the simulation result, a prototype of the TCB structure having dimension 210 mm × 210 mm is fabricated, and its photograph is shown in Fig. 20(a). The measurements are taken in an anechoic environment using two wideband horn antennas and VNA R&S ZVB20. The antennas are separated by some distance, and the absorbers are placed in between them to avoid the mutual coupling effect. The antennas should be placed at a proper distance from the target to ensure the plane wave excitation. The calculated far field distance ( $R = 2D^2/\lambda$ , where  $D$  is the diagonal dimension of the structure (297 mm)) is approximately 7 m at 12 GHz. Due to the setup limitation, the measurements are taken up to 5 GHz ( $R = 3$  m) [28]. Time gating is also applied for better accuracy. The measurement setup is shown in Fig. 20(b).

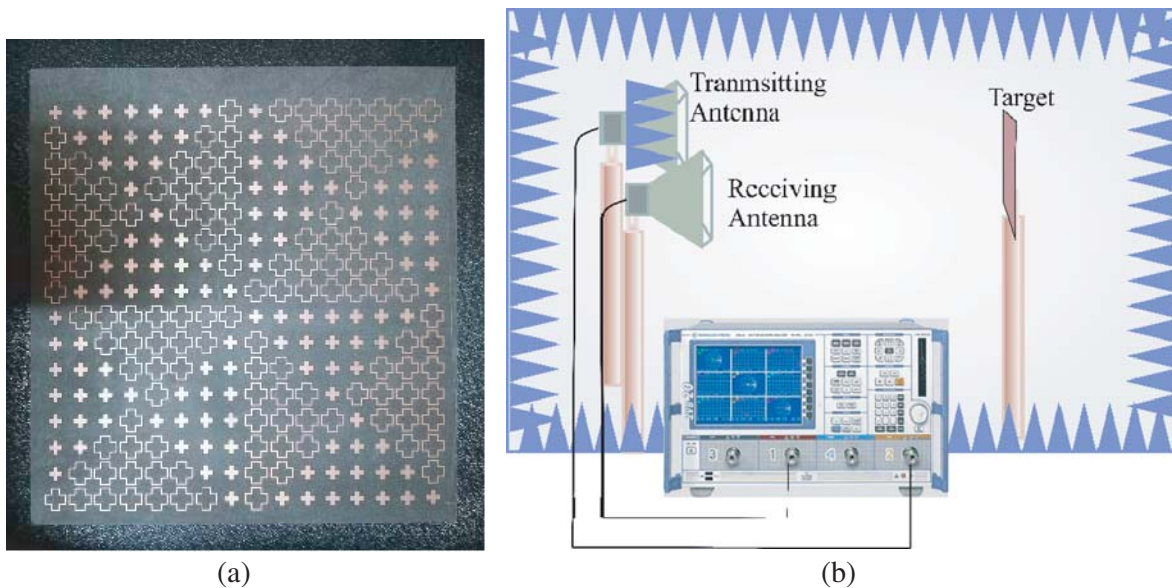


**Figure 20.** (a) Photograph of the fabricated prototype. (b) Measurement setup.

The reflected power from the structure and similar metal plate is measured, and the obtained RCS reduction is depicted in Fig. 21. The slight variation in measured result as compared to simulation may be due to the fabrication error tolerance.

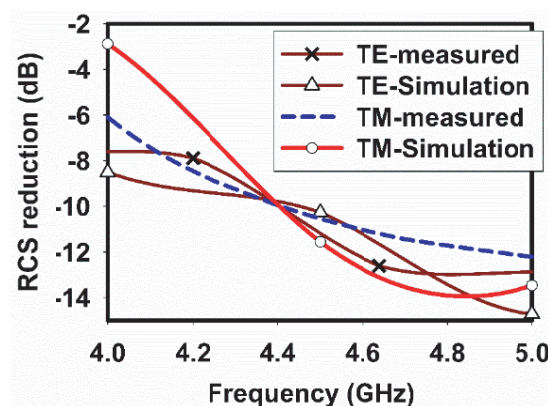


**Figure 21.** Comparison of simulated and measured RCS reduction as a function of frequency.

## 5. CONCLUSION

A combinatorial triangular checkerboard surface consisting of a single band AMC (AMC-I) and dual band AMC (AMC-II) exhibiting wideband RCS reduction is presented in this article. 10 dB RCS reduction bandwidth of 91% is obtained from this structure. The performance of the structure is compared with conventional checkerboard surface having the same dimension. The scattered fields are concentrated to four and eight major lobes for conventional and triangular checkerboard surfaces, respectively. The scattered field is reduced by 6.43 dB for triangular surface as compared to conventional structure in boresight direction at 10.5 GHz. A prototype of the proposed structure is fabricated, and the measured RCS reduction is in good agreement with the simulation.

## ACKNOWLEDGMENT

Authors would like to acknowledge the financial and infrastructural support from University Grants Commission and Department of Science and Technology, Government of India. The authors also would like to thank Rogers Corporation for providing the substrate by University samples program.

## REFERENCES

1. Knott, E. F., M. T. Tuley, and J. F. Shaeffer, *Radar Cross Section*, 2nd edition, SciTech Publishing, Inc., Raleigh, NC, USA, 2004.
2. Sievenpiper, D., L. Zhang, R. Broas, N. Alexopolous, and E. Yablonovitch, "High impedance electromagnetic surfaces in a forbidden frequency band," *IEEE Trans. Microw. Theory Tech.*, Vol. 47, No. 11, 2059–2074, Nov. 1999.
3. Tran, H. H. and I. Park, "Wideband circularly polarized low-profile antenna using artificial magnetic conductor," *Journal of Electromagnetic Waves and Applications*, Vol. 30, No. 7, 889–897, 2016.
4. Feresidis, A. P., G. Goussetis, S. Wang and J. C. Vardaxoglou, "Artificial magnetic conductor surfaces and their application to low-profile high-gain planar antennas," *IEEE Transactions on Antennas and Propagation*, Vol. 53, No. 1, 209–215, Jan. 2005.
5. Costa, F. and A. Monorchio, "Electromagnetic absorbers on high impedance surfaces: From ultra narrowband to ultra wideband absorption," *Advanced Electromagnetics*, Vol. 1, No. 3, 7, Oct. 2012.
6. Landy, N. I., S. Sajuyigbe, J. J. Mock, D. R. Smith, and W. J. Padilla, "Perfect metamaterial absorber," *Phys. Rev. Lett.*, Vol. 23, 207402, 2008.
7. Fernández Álvarez, H., et al., "A six-fold symmetric metamaterial absorber," *Materials*, Vol. 8, No. 4, 1590–1603, 2015.
8. Shang, Y., Z. Shen, and S. Xiao, "On the design of single-layer circuit analog absorber using double-square-loop array," *IEEE Transactions on Antennas and Propagation*, Vol. 61, No. 12, 6022–6029, Dec. 2013.
9. Li, M., S. Xiao, Y. Y. Bai, and B. Z. Wang, "An ultrathin and broadband radar absorber using resistive FSS," *IEEE Antennas and Wireless Propagation Letters*, Vol. 11, 748–751, 2012.
10. Paquay, M., J.-C. Iriarte, I. Ederra, R. Gonzalo, and P. de Maagt, "Thin AMC structure for radar cross-section reduction," *IEEE Transactions on Antennas and Propagation*, Vol. 55, No. 12, Dec. 2007.
11. Galarregui, J. C. I., A. T. Pereda, J. L. M. De Falcon, I. Ederra, R. Gonzalo, and P. de Maagt, "Broad band radar cross section reduction using AMC technology," *IEEE Transactions on Antennas and Propagation*, Vol. 61, No. 12, Dec. 2013.
12. Chen, W., C. A. Balanis, and C. R. Birtcher, "Checker board EBG surfaces for wideband radar cross section reduction," *IEEE Transactions on Antennas and Propagation*, Vol. 63, No. 6, Jun. 2015.
13. Chen, W., C. A. Balanis, and C. R. Birtcher, "Dual wide-band checkerboard surfaces for radar cross section reduction," *IEEE Transactions on Antennas and Propagation*, Vol. 64, No. 9, 4133–4138, Sept. 2016.

14. Hong, T., H. Dong, J. Wang, H. Ning, Y. Wei, and L. Mao, "A novel combinatorial triangle-type AMC structure for RCS reduction," *Microw. Opt. Technol. Lett.*, Vol. 57, 2728–2732, 2015.
15. Zhuang, Y.-Q., G.-M. Wang, and H.-X. Xu, "Ultra-wideband RCS reduction using novel configured chessboard metasurface," *Chinese Physics B*, Vol. 26, No. 5, 054101, 2017.
16. Cui, T. J., M. Q. Qi, X. Wan, J. Zhao, and Q. Cheng, "Coding metamaterials, digital metamaterials and programmable metamaterials," *Light: Science & Applications*, Vol. 3, 1–9, 2014.
17. Liu, X., J. Gao, L. Xu, X. Cao, Y. Zhao, and S. Li, "A coding diffuse metasurface for RCS reduction," *IEEE Antennas and Wireless Propagation Letters*, Vol. 16, 724–727, 2017.
18. Han, T., X.-Y. Cao, J. Gao, Y.-L. Zhao, and Y. Zhao, "A coding metasurface with properties of absorption and diffusion for RCS reduction," *Progress In Electromagnetics Research C*, Vol. 75, 181–191, 2017.
19. Zhuang, Y., et al., "Random combinatorial gradient metasurface for broadband, wide-angle and polarization-independent diffusion scattering," *Scientific Reports*, Vol. 7, Article number: 16560, 2017.
20. Costa, F., A. Monorchio, and G. Manara, "Wideband scattering diffusion by using diffraction of periodic surfaces and optimized unit cell geometries," *Scientific Reports*, Vol. 6, 25458, 2016.
21. Zheng, Q., Y. Li, J. Zhang, et al., "Wideband, wide-angle coding phase gradient metasurfaces based on Pancharatnam-Berry phase," *Scientific Reports*, Vol. 7, 43543, 2017.
22. Modi, A. Y., C. A. Balanis, C. R. Birtcher, and H. N. Shaman, "Novel design of ultrabroadband radar cross section reduction surfaces using artificial magnetic conductors," *IEEE Transactions on Antennas and Propagation*, Vol. 65, No. 10, 5406–5417, Oct. 2017.
23. De Cos, M. E., Y. Alvarez, and F. Las-Heras, "A novel approach for RCS reduction using a combination of artificial magnetic conductors," *Progress In Electromagnetics Research*, Vol. 107, 147–159, 2010.
24. De Cos, M. E., Y. Alvarez-Lopez, and F. Las Heras Andres, "On the influence of coupling AMC resonances for RCS reduction in the SHF band," *Progress In Electromagnetics Research*, Vol. 117, 103–119, 2011.
25. Balanis, C. A., *Antenna Theory: Analysis and Design*, 3rd Edition, Wiley, Hoboken, NJ, USA, 2005.
26. Costa, F., S. Genovesi, and A. Monorchio, "On the bandwidth of high-impedance frequency selective surfaces," *IEEE Antennas and Wireless Propagation Letters*, Vol. 8, 1341–1344, 2009.
27. De Cos, M. E. and F. Las-Heras, "On the advantages of loop-based unit-cell's metallization regarding the angular stability of artificial magnetic conductors," *Applied Physics A*, Vol. 118, No. 2, 699–708, 2015.
28. Álvarez, Y., M. E. de Cos, and F. Las-Heras, "RCS measurement setup for periodic-structure prototype characterization," *IEEE Antennas and Propagation Magazine*, Vol. 52, No. 3, 100–106, Jun. 2010.